

## Investigation of Three-Dimensional Shock Control Bumps for Transonic Buffet Alleviation

D'aguanno, Alessandro; Schrijer, Ferry; Oudheusden, Bas van

**DOI**

[10.2514/1.J062633](https://doi.org/10.2514/1.J062633)

**Publication date**

2023

**Document Version**

Final published version

**Published in**

AIAA Journal

**Citation (APA)**

D'aguanno, A., Schrijer, F., & Oudheusden, B. V. (2023). Investigation of Three-Dimensional Shock Control Bumps for Transonic Buffet Alleviation. *AIAA Journal*, 61(8), 3419-3431. <https://doi.org/10.2514/1.J062633>

**Important note**

To cite this publication, please use the final published version (if applicable).  
Please check the document version above.




**Copyright**

Other than for strictly personal use, it is not permitted to download, forward or distribute the text or part of it, without the consent of the author(s) and/or copyright holder(s), unless the work is under an open content license such as Creative Commons.

**Takedown policy**

Please contact us and provide details if you believe this document breaches copyrights.  
We will remove access to the work immediately and investigate your claim.

# Investigation of Three-Dimensional Shock Control Bumps for Transonic Buffet Alleviation

Alessandro D'Aguanno,\* Ferry Schrijer,<sup>†</sup> and Bas van Oudheusden<sup>‡</sup>  
Delft University of Technology, 2629 HS Delft, The Netherlands

<https://doi.org/10.2514/1.J062633>

This experimental study investigates the use of shock control bumps (SCBs) for controlling transonic buffet. Three-dimensional SCBs have been applied on the suction side of an OAT15A supercritical airfoil with the experiments conducted in the transonic-supersonic wind tunnel of Delft University of Technology at fully developed buffet conditions ( $Ma = 0.7$ ,  $\alpha = 3.5$  deg and  $Re = 2.6 \times 10^6$ ). The effectiveness of the SCBs for different spanwise array spacings (ranging from 20 to 30% $c$ ) was verified using two optical techniques: schlieren visualization and particle image velocimetry. Both techniques confirmed the potential of controlling buffet using such devices, resulting in a reduction of the flow unsteadiness in terms of both shock oscillation and pulsation of the separated area. A dedicated particle image velocimetry investigation in a spanwise-chordwise measurement plane was conducted in order to characterize the effect of the spatial distribution of the bumps, focusing on the interaction of the shock-wave structures along the span. The configuration with a spacing of  $\Delta y_{SCB} = 25\%c$  was demonstrated to be the most efficient in reducing the transonic buffet oscillations and was able to reduce the reverse flow region size as compared to the clean configuration.

## I. Introduction

THE operation of a civil aircraft is limited by the occurrence of shock-wave oscillations on the suction side of a wing, which are referred to as transonic buffet and occur for flow conditions that comprise a specific range of angle of attack as well as a Mach and Reynolds number combination. These oscillations are undesirable because they could eventually result in failure of the wing due to fatigue, as well as incurring the oscillation of aerodynamic performance properties. Therefore, for safety reasons, the flight envelope of an aircraft is limited so as not to encounter transonic buffet. The first studies on transonic buffet were performed by Hilton and Fowler [1] in 1947; despite this, the mechanism behind this phenomenon has not been completely understood yet. In 1990, Lee [2] was the first author to describe transonic buffet as a feedback mechanism, in which the shock-wave (SW) oscillation is sustained by the occurrence of downstream-traveling waves (DTWs) that move from the shock foot to the trailing-edge area and upstream-traveling waves (UTWs); which are induced in reaction to the DTWs that, by moving in the direction of the shock wave, allow the SW to move downstream or upstream, according to the buffet phase. This model has subsequently been updated by different researchers, such as Jacquin et al. [3], who considered the UTWs capable of reaching the SW along both the suction and pressure sides. Recently, a dedicated study undertaken by Hartmann et al. [4] has clarified that the UTWs are acoustic waves that propagate with a velocity of 80 m/s relative to the airfoil, whereas D'Aguanno et al. [5] has suggested that the strength of the UTWs is modulated throughout the buffet cycle. A crucial contribution to the understanding of transonic two-dimensional (2-D) buffet has been given by Crouch et al. [6], in which transonic buffet was described as the result of a modal instability, obtaining values for the buffet onset

that are in perfect agreement with the experimental data. Similar results were obtained from the stability analysis of Sartor et al. [7].

Because of the relevance of transonic buffet to safe aircraft operation in the high-subsonic regime, it is of paramount importance to be able to control or, whenever possible, suppress the phenomenon. In the last 20 years, there have been many attempts to control transonic buffet, as summarized in the relatively complete review paper of Giannelis et al. [8]. Two different strategies of control systems can be distinguished: an active or a passive control system. The first system is very attractive for its precision and efficiency, but it is generally very complex to realize and implement. An example of an active control system was given in studies from ONERA [9,10], where the movement of trailing-edge deflectors was actuated according to the instantaneous static pressure in order to stabilize the shock oscillation. More recently, Ren et al. [11] achieved a closed-loop control of trailing-edge static deflectors (TEDs) by using an adaptive control strategy based on a neural network.

However, in many applications, the reliability of the control system may have preference, for which passive control systems are more attractive. The different systems are designed in such a way that the unsteadiness is either reduced or moved to higher angles of attack and/or to higher Mach numbers (moving the buffet onset boundary). These control systems are generally designed with the goal of damaging the feedback mechanism, accordingly placing the control systems in the shock oscillation area or at the trailing edge. An example of the latter is the use of trailing-edge static deflectors, which were used by Lee [12] and Despre et al. [13], who both considered trailing-edge flaps with a static downward deflection to control transonic buffet. A particular type of TED is the use of a flap with a vertical/upward deflection at the trailing edge (upper trailing-edge flap) [14,15], which has been demonstrated as effective in reducing transonic buffet unsteadiness by damaging the communication between DTWs and the trailing edge.

Another possibility is the use of a vortex generator [10] that energizes the boundary layer, promoting attached flow, and therefore inhibiting the shock induced separation. An advanced form of vortex generator is the fluidic vortex generator, which could be successfully used to control transonic buffet in the form of an air jet, as in the work of Brion et al. [16].

A common system used for the control of both transonic and supersonic shock interactions is achieved by using a shock control bump (SCB), which is a type of device that has been extensively described in the review of Bruce and Colliss [17]. SCBs have been used for different applications, such as for the control of transonic flows on wings and airfoils [18]; for the control of shock-wave/boundary-layer interaction, as in the studies of Holden and Babinsky

Presented as Paper 2021-2558 at the AIAA AVIATION 2021 Forum, Virtual Event, August 2–6, 2021; received 10 November 2022; revision received 3 March 2023; accepted for publication 5 March 2023; published online 7 April 2023. Copyright © 2023 by the authors. Published by the American Institute of Aeronautics and Astronautics, Inc., with permission. All requests for copying and permission to reprint should be submitted to CCC at [www.copyright.com](http://www.copyright.com); employ the eISSN 1533-385X to initiate your request. See also AIAA Rights and Permissions [www.aiaa.org/randp](http://www.aiaa.org/randp).

\*Postdoctoral Researcher, Aerodynamics Section, Department of Flow Physics and Technology; A.Daguanno@tudelft.nl (Corresponding Author).

<sup>†</sup>Assistant Professor and Scientific Director of Flow Physics and Technology Laboratory, Aerodynamics Section, Department of Flow Physics and Technology.

<sup>‡</sup>Associate Professor, Aerodynamics Section, Department of Flow Physics and Technology.

[19] and Bruce and Babinsky [20]; and as a flow control device in supersonic engine intakes [21]. On transonic airfoils, a SCB is generally placed on the suction side, and it consists of a ramp and a tail section oriented in the direction of the flow. Ogawa et al. [18] and Colliss et al. [22] have shown that three-dimensional (3-D) shock control bumps are more efficient than 2-D SCBs (which were extensively described by Zhang et al. [23]), particularly in off-design conditions, thanks to the streamwise vortices developing from the tail of a bump. The two possible working principles of 3-D SCBs are associated with the formation of a  $\lambda$ -shock structure instead of the traditional quasi-normal shock wave and the formation of a localized region of attached flow downstream of the shock-wave location, thanks to the vortex development.

Regarding the design of SCBs, the study of Colliss et al. [24] also proved that a joint experimental and numerical approach can be used to achieve a relatively inexpensive parametric study of the effects of the geometry of 3-D SCBs on the flow physics. Among the different shapes of SCBs, one of the most common is the narrow wedge SCB (described by Colliss et al. [22] and Mayer et al. [25]), which is characterized by a flat ramp, crest, and tail, as well as by angular side flanks. Three-dimensional SCBs on airfoils have been also employed for drag reduction applications, as in the work of Deng and Qin [26], where 3-D SCBs were integrated with vane-type vortex generators to suppress flow separation. A similar application was also pursued in the study of Jones et al. [27] on swept wings.

Because of its properties, a SCB can also be used as a “smart” vortex generator and applied to transonic buffet control, as shown by Eastwood and Jarrett [28] or Tian et al. [29], where two different types of SCBs proved to be effective in controlling transonic buffet. The study of Mayer et al. [30] also proved the effectiveness of SCBs for controlling transonic buffet on swept wings (for which the physics is quite different from 2-D buffet on straight wings, as shown in the work of Paladini et al. [31]). For 2-D SCBs, Birkemeyer et al. [32] proposed that these devices could postpone the transonic buffet onset on wings when placed in between the shock-wave location and the trailing edge, although bringing to an increase in drag.

Despite these reported successful implementations, the usefulness of 3-D SCBs for controlling transonic buffet on an airfoil is not univocal [33] and depends on the SCB size and position, as shown by the numerical study of Geoghegan et al. [34]. Hence, to achieve an efficient control system, the location of SCBs on the airfoil should be selected carefully. For steady applications, the quasi-normal shock wave should be located in correspondence of the crest of the bump; in this way, no reexpansion or second shock wave would occur, as described by Bruce and Babinsky [20]. For transonic buffet, Geoghegan et al. [34] showed that SCBs are effective when their crest is placed within  $\pm 5\%c$  of the mean shock-wave position (with SCBs located slightly downstream of the average shock-wave position, which also brings an increase in lift). Thus, the range of streamwise locations for which the SCBs are useful is larger than in steady applications.

Another relevant aspect associated with 3-D SCBs is the curvature of the leading-edge oblique shock wave around the bump: a phenomenon that was described by Ogawa et al. [18]. When a spanwise array of bumps is used, overlapping shock structures appear, with the effectiveness of this interaction highly dependent on the relative spacing between the bumps; thus, the spacing parameter should also be optimized.

With the present study, the authors aim to document and further clarify the influence and effectiveness of 3-D SCBs on transonic buffet: to reach this goal, an experimental study was carried out, employing two complementary optical diagnostic techniques. Schlieren visualizations were used to provide a qualitative description of the shock dynamics, whereas a more detailed quantification of the velocity field was achieved with particle image velocimetry (PIV). Particular attention was also given to characterize the effect of the bump spacing, for which a detailed PIV study on a plane parallel to the suction side of the airfoil was performed, for different spacings between the bumps. To the best of the authors' knowledge, no detailed study on the bump spacing has been previously reported, except for the study of König et al. [35] for a swept wing (where the optimal spacing was mainly influenced by

the value of the sweep angle) and in the study of Eastwood and Jarrett [28] for lift and drag improvement applications.

## II. Experimental Investigation

### A. Facility and Models

The experiments were carried out in the TST-27, which is a transonic-supersonic blowdown wind tunnel of the Delft University of Technology with a test section that 25 cm high and 28 cm wide. The wind tunnel was operated for transonic conditions at a total pressure of  $p_0 = 2$  bars and a total temperature of  $T_0 = 288$  K (the main flow conditions are summarized in Table 1).

Two models have been used in the experiments, which were both based on the OAT15A airfoil, which is a supercritical airfoil widely used for transonic buffet research [3]. Both models have a chord  $c$  of 10 cm, but they differ in span as summarized in Table 2. The first has a width of 28 cm and spans the entire test section, being clamped on both sides of the wind tunnel (Fig. 1, left), and it is referred to as the “horizontal” airfoil. The second model, referred to as the “vertical” airfoil, has a span of 20 cm and, in operational conditions, is oriented in the wind tunnel vertically, with the suction side parallel to the sidewall of the tunnel. This model, which is attached to one of the sidewalls of the wind tunnel by means of pylons (as shown in Fig. 1, right), has previously been investigated in the study reported by D'Agunno et al. [5]. To eliminate any additional tip vortex effects, two side plates (fences) were mounted in correspondence with the two extremities of the airfoil (see Fig. 1, right). For both models, a 2%  $c$  wide transition trip was applied at 7% of the chord in order to ensure a fully turbulent boundary layer, similar to many other experimental studies of this airfoil [3,36]. All the tests have been performed for  $Ma = 0.7$ ,  $\alpha = 3.5$  deg, and  $Re_c = 2.6 \times 10^6$ : conditions for which the buffet was demonstrated to be fully developed by D'Agunno et al. [36].

### B. Shock Control Bump Geometry

The SCBs used in this study have been produced with a 3-D printer in polylactic acid material with an accuracy of  $20 \mu\text{m}$ . The use of SCBs in shock-wave/boundary-layer interactions in the literature is widespread; nevertheless, there is not much information regarding their geometrical design and location. Designing a new geometry of SCBs is out of the scope of this study; therefore, the SCB design was based on the SCB geometries present in other studies in the literature [22,25].

The geometry and dimensions of the realized SCB are shown in Fig. 2, with an overall length of 28 mm and a maximum height of 0.9 mm. Following the design scaling suggested in the literature [17], the height of the bumps (including the double-sided adhesive tape with which the bumps are attached to the airfoil, which has a thickness of 0.13 mm) has been selected as equal to the local height of

Table 1 Flow conditions

Parameter	Symbol	Value	Unit
Freestream Mach number	$Ma_\infty$	0.7	—
Freestream velocity	$U_\infty$	225	m/s
Total temperature	$T_0$	288	K
Total pressure	$p_0$	2	bar

Table 2 Model parameters

Parameter	Symbol	Value	Unit
Chord	$c$	10	cm
Span (horizontal model)	$b_1$	28	cm
Span (vertical model)	$b_2$	20	cm
Angle of attack	$\alpha$	3.5	deg
Reynolds number based on chord	$Re_c$	$2.6 \times 10^6$	—

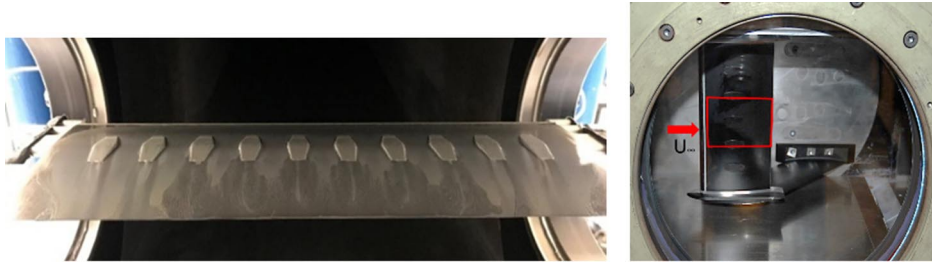


Fig. 1 SCBs (spacing 25% $c$ ) mounted on the horizontal OAT15A airfoil, with oil flow visualization ( $Ma = 0.7$ ,  $\alpha = 3.5$  deg) on the left and the vertical airfoil mounted in the wind tunnel with the relative FOV (right).

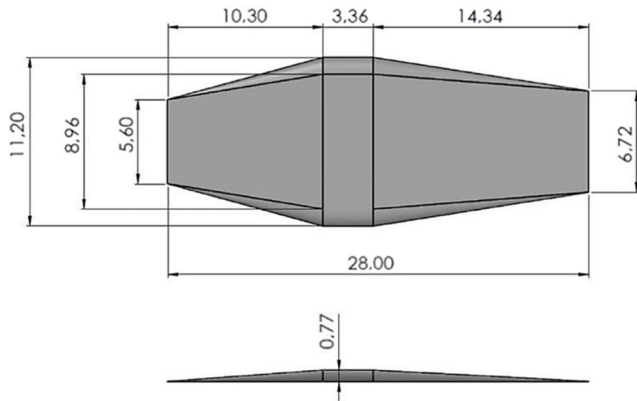


Fig. 2 Geometry of a shock control bump with dimensions in millimeters.

the boundary layer, which was evaluated for an equivalent flat plate. The crest of the bump has been centered at the average shock location for the most developed buffet condition ( $Ma = 0.7$  and  $\alpha = 3.5$  deg), which corresponds to approximately 45% of the chord. It is expected that for this buffet condition, the oscillating shock wave will acquire the familiar  $\lambda$  structure, stabilizing the shock oscillation.

The spanwise spacing between the bumps is a crucial parameter because it determines if the interaction among the different shock-wave structures in correspondence with the bumps will be detrimental or beneficial. Because there is no evidence in the literature of a systematic study of this parameter, a range of spacings  $\Delta y_{SCB}$  has been tested, namely, 20, 22.5, 25, 27.5, and 30% $c$  (selected in the range of values reported in other publications [18,25]).

Figure 1 (left) shows the oil flow visualization on the OAT15A airfoil model with bumps after a run at  $Ma = 0.7$  and  $\alpha = 3.5$  deg for a spacing between the bumps of 25 mm ( $\Delta y_{SCB} = 25\%c$ ).

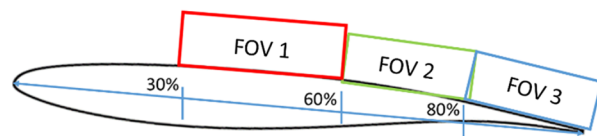
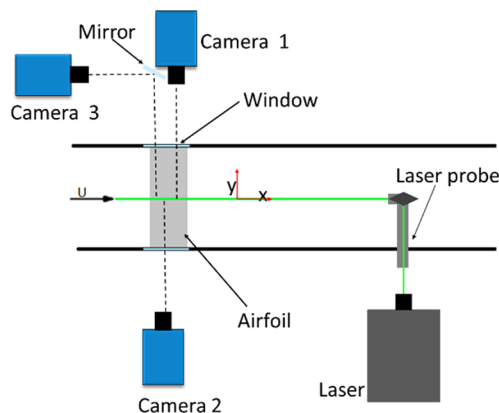


Fig. 3 First PIV configuration: PIV setup (left) and sketch of airfoil with FOVs used (right).

### C. Experimental Setup

In this study, high-speed schlieren and particle image velocimetry have been used as optical diagnostic techniques. High-speed schlieren was used to visualize the shock dynamics for different bump spacings for the horizontal model (airfoil clamped on the sidewalls of the wind tunnel). For this purpose, a high-speed camera (Photron Fastcam SA1.1) was used with an exposure time of 10  $\mu$ s and an acquisition frequency of 5 kHz, which are sufficient to resolve the shock oscillation motion, which occurs at a characteristic frequency of 160 Hz [36]. The schlieren had the conventional  $z$  configuration with a pinhole diameter of 2 mm and included a continuous 24 W lamp. A quantitative analysis of the velocity field was subsequently performed with PIV using two different experimental configurations.

In the first configuration, high-speed PIV was carried out for the horizontal airfoil using three high-speed cameras (three Photron Fastcam SA1.1). All these measurements were performed in the chordwise-vertical plane at midspan ( $y/c = 0$ ), in correspondence with the central bump. An acquisition frequency of 15 kHz was selected in order to temporally resolve the shock position and the separated area dynamics. To achieve this acquisition frequency, the sensor of each camera (operating in double-pulse mode with a time separation of  $dt = 3 \mu$ s) was cropped to a resolution of  $576 \times 320$  pixels. Despite this, a good spatial resolution was still achieved by simultaneously using three cameras in planar mode. Each camera was fitted with a 180 mm lens with an  $f$  stop of four. To insert the three cameras and lenses into a relatively narrow area, a mirror was used, as shown in the sketch of the setup in Fig. 3 (left). As a result, the first field of view (FOV) was extended from 28 to 61% $c$  (thus including the entire range of the shock-wave oscillation), FOV<sub>2</sub> was from 59 to 81% $c$ , and FOV<sub>3</sub> was from 79 to 101% $c$ . The vertical extents (along  $z$ ) of the FOVs were of roughly 17% $c$  for FOV<sub>1</sub> and 12% $c$  for the other two FOVs. A sketch of the different FOVs is given in Fig. 3 (right).

To appreciate the spanwise distribution of the shock wave, a further PIV experiment (second PIV configuration) was completed in a spanwise-chordwise-oriented plane using the vertical model configuration, which allowed direct access from the side window toward

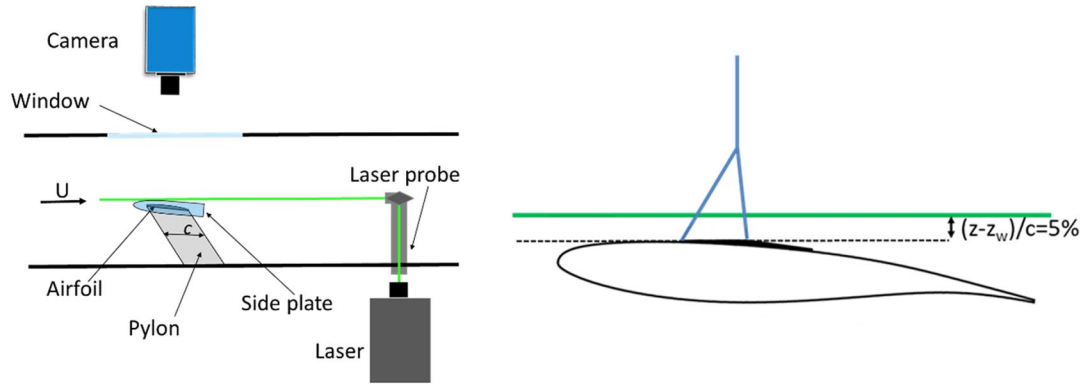


**Fig. 4** Second PIV configuration: top view of PIV setup (left) and sketch of the airfoil with the plane of measurement in green and the indicative  $\lambda$ -shock structure in blue (right).

the suction side of the airfoil (Fig. 4, left). One high-speed camera (again, a Photron Fastcam SA1.1) in the planar configuration was used, with a selected frequency of acquisition of 4.65 kHz (camera sensor cropped to  $1024 \times 640$  pixels), and fitted with a 105 mm lens with an  $f$  stop of eight. These settings resulted in a FOV extending from  $15\%c$  to the trailing edge along the streamwise direction and from  $-26$  to  $26\%c$  in the spanwise direction with respect to the model centerline. Similar to the first PIV configuration, the camera was operated in double-pulse mode with  $dt = 3 \mu s$ . As illustrated in Fig. 4 (right), the plane of measurement was located at a vertical distance of  $z - z_w(x_{thick}) = 5\%c$  ( $5 \text{ mm}$ ) from the thickest point of the airfoil  $[z_w(x_{thick})]$ .

For both PIV configurations, a dual-cavity high-speed laser (neodymium-doped yttrium aluminum garnet, Nd:YAG) and additional optics were used to create a laser sheet of  $1.5 \text{ mm}$  in thickness. The laser sheet illuminated the seeding particles, which in this study were diethyl-hexyl-sebacate (DEHS) droplets, which follow the flow accurately (with the exception of the immediate shock-wave region) in view of the relatively low relaxation time ( $\tau_{DEHS} = 2 \mu s$ ). The synchronization between the cameras and the laser was achieved through a synchronization box (LaVision high-speed controller, part number 1108075).

#### D. Processing Parameters

The schlieren images were acquired with Photron FASTCAM Viewer (version 3) camera software and then processed in MATLAB, whereas the image acquisition for the PIV measurements was performed with LaVision's Davis software (version 8.4.0). The same software was used for image preprocessing and processing (computation of velocity fields by means of a cross-correlation procedure), whereas further processing was carried out in MATLAB. For the PIV image processing, first, a Butterworth filter was applied to reduce the laser reflections on the airfoil and on the SCBs (using a filter length of seven images [37]); subsequently, the cross correlation was computed with a multipass approach. For the measurements with the horizontal airfoil, one pass with a window size of  $64 \times 64$  pixels ( $2.5 \times 2.5 \text{ mm}$ ) and three passes with a final window size of  $48 \times 48$  pixels ( $1.9 \times 1.9 \text{ mm}$ ) were adopted: in both cases, with an overlap of  $75\%$  of the window size. On the other hand, for the second PIV configuration, one pass with a window size of  $48 \times 48$  pixels ( $4.0 \times 4.0 \text{ mm}$ ) and three passes with a final window size of  $32 \times 32$  pixels ( $2.7 \times 2.7 \text{ mm}$ ) were selected, again with an overlap of  $75\%$ . Correspondingly, the resulting spacing between the vectors was  $0.47\%c$  ( $0.47 \text{ mm}$ ) for the first PIV configuration and  $0.67\%c$  ( $0.67 \text{ mm}$ ) for the images on the vertical airfoil. The main PIV processing settings are also summarized in Table 3.

#### E. Uncertainty Analysis

An uncertainty analysis is carried out to verify whether the differences in performance of the SCBs observed in the measurements can be considered (statistically) significant. The most important experimental uncertainty sources are briefly discussed in the

**Table 3** PIV parameters and uncertainties

Parameter	First PIV configuration	Second PIV configuration
Model orientation	Horizontal	Vertical
Acquisition frequency, kHz	15	4.65
Pulse separation, $\mu s$	3	3
Number of images	15,500	4,365
Final resolution, pixels	$1,600 \times 320$	$1,024 \times 640$
Final window size, pixels	$48 \times 48$	$32 \times 32$
Window overlap, %	75	75
Vector spacing	$0.47\%c$ ( $0.47 \text{ mm}$ )	$0.67\%c$ ( $0.67 \text{ mm}$ )
Magnification	0.45	0.24
Cross-correlation uncertainty, m/s	$<4$	$<10$
Particle slip uncertainty, m/s	$<40$ (SCBs)-60 (clean)	$<40$ (SCBs)-60 (clean)

following, and the corresponding values are reported in Table 3; for a more detailed derivation, the reader is referred to the work of D'Agunno et al. [36].

A primary source of uncertainty in PIV is associated with the accuracy of the correlation procedure, with which the velocity vectors are obtained from the raw image data (cross-correlation uncertainty; see the work of Humble [38]). The values in Table 3 show that the corresponding uncertainty on the instantaneous velocity amounts to  $2\text{--}4\%$  of the freestream velocity, with the uncertainty being higher for the PIV data obtained for the vertical model because, in this case, a lower magnification  $M$  is present than for the horizontal model.

The inertia of the tracer particles introduces a particle slip effect due to the finite response time of the particles [39]. This effect is particularly important near shock-wave structures, reaching theoretical values of uncertainty of  $60 \text{ m/s}$  for the clean configuration and  $40 \text{ m/s}$  for the SCB configurations. The reduction of this uncertainty for the SCB configuration is associated with the presence of two jumps in velocity across each of the SW structures instead of the single more intense jump observed for the clean configuration. Notwithstanding the high values of uncertainty across the shock waves, the particle slip effect is negligible in the remaining FOV.

Regarding the schlieren measurements, the major source of uncertainty is associated with the tracking of the shock-wave position, for which half of the apparent width of the normal shock wave can be used as an indicator (less than  $3 \text{ mm}$ ).

### III. Shock Dynamics

In Fig. 5, instantaneous schlieren images are shown for both the clean airfoil (right) and the SCB configuration with a spanwise spacing of  $25\%c$  (left). In the latter, two oblique black lines appear in the image; going from left to right, the first is associated with a Mach line caused by the transition trip that is located at  $7\%$  of the chord, whereas the second is an oblique shock wave created at the



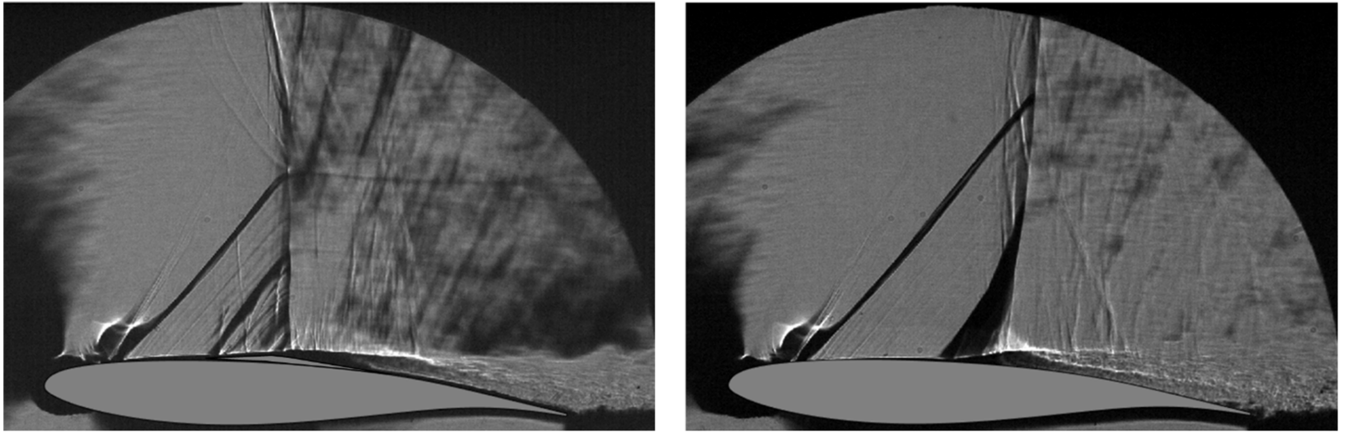


**Fig. 5** Examples of schlieren images of the OAT15A at  $Ma = 0.7$  and  $\alpha = 3.5$  deg with bumps (left) and without bumps (right), with the shock wave in its upstream movement.

leading edge of the bumps, followed by a quasi-normal shock wave (forming a  $\lambda$ -shock structure). Inside the  $\lambda$  shock wave, additional “thinner” oblique lines, associated with 3-D structures integrated along the span of the model, are observable. In correspondence with the interactions of the quasi-normal shock wave with the Mach line and the oblique SW, two slip lines are observed. Downstream of the shock wave, the presence of a separated area can also be qualitatively visualized, thanks to the horizontal orientation of the schlieren knife edge. A quantitative estimation of the separated area is, however, not possible in view of the spanwise integration of the density gradients. For the clean airfoil (Fig. 5, right), the lambda shock wave is substituted by a single shock-wave structure. Both schlieren images correspond to the phase in the buffet cycle in which the shock wave travels upstream, which is when a wide separated area develops, extending from the shock foot downstream (as exhaustively described in the literature [3,36]). As a result, the shock wave appears slightly inclined for the clean configuration. In this paper, the buffet phases will not be used for phase-averaging purposes; however, for more details, the interested reader is referred to Ref. [36].

For comparison, in Fig. 6, instantaneous PIV images in the chordwise-vertical plane are shown for both the clean (right) and the SCB configurations with  $\Delta y_{SCB} = 25\%c$  (left). These images are capturing approximately the same phase as the schlieren images of Fig. 5, so when the shock wave is moving upstream. For the clean configuration, a single moving oblique shock wave is observed at  $35\%c$ ; whereas for the controlled configuration (as already commented on for the schlieren images), there is both a steady oblique shock wave in correspondence with the leading edge of the bumps and a secondary unsteady shock wave close to  $x \approx 45\%c$ . The velocity fields confirm the qualitative schlieren information of the presence of a wide separated area in this buffet stage (with the reverse flow area indicated by the black contour line in Fig. 6) developing from the shock foot. It is worth clarifying that these PIV data have been acquired in the symmetry plane of the airfoil, which coincides with the symmetry line of the central bump for the SCB configurations; whereas the schlieren data integrate all the density gradients present along the line of sight.

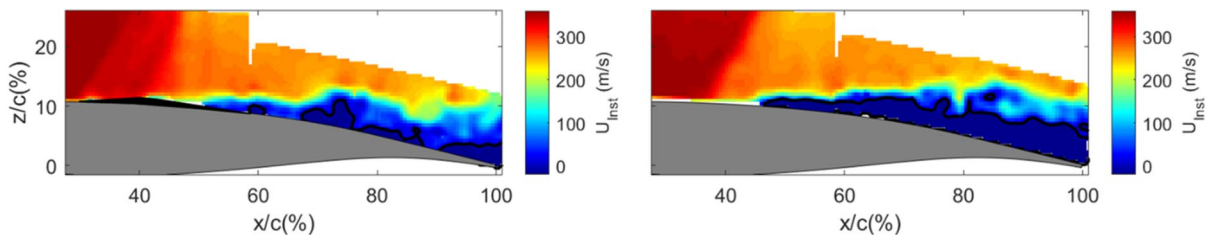


**Fig. 6** Examples of PIVs image of the OAT15A at  $Ma = 0.7$  and  $\alpha = 3.5$  deg with bumps (left) and without bumps (right), with the black contour line indicating the reverse flow area.

From the schlieren recordings, the shock position has been tracked in time. In view of the presence of the leading-edge shock wave for the SCB configuration, the shock position could not be tracked by evaluating the minimum of the luminosity intensity in each image; whereas, thanks to the quasi-normal (rear) shock-wave orientation, the shock wave has been tracked by looking for the minimum of a vector  $a = (a_1, a_m, \dots, a_M)$ , where  $M$  is the number of columns of a schlieren image and  $a_m$  is the sum of the luminosity intensity of all the pixels of the  $m$ -th column of a given schlieren image. The method was demonstrated to be reliable in tracking the shock position for both the clean and the SCB configurations.

In Fig. 7, the time behavior of the shock-wave position is shown for both the clean and the  $\Delta y_{SCB} = 25\%c$  configurations for  $\Delta t = 0.2$  s (about 32 buffet cycles) and clearly illustrates a reduction of the shock-wave oscillation range in the presence of SCBs. The image clarifies that the most downstream position of the shock wave is not highly affected by the presence of SCBs, whereas there is a strong difference for the location of the most upstream shock-wave position.

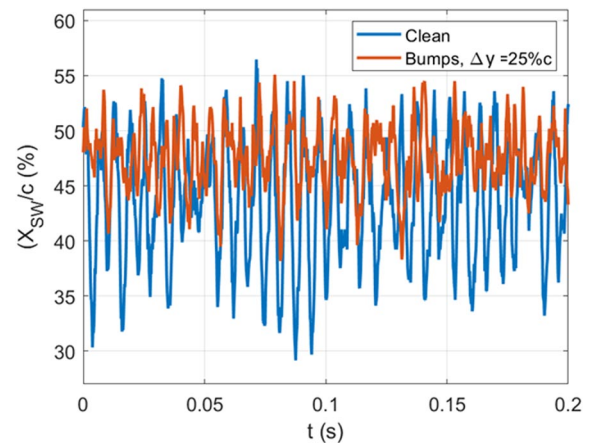


**Fig. 7** Time behavior of shock-wave position for clean and  $\Delta y_{SCB} = 25\%c$  configurations.

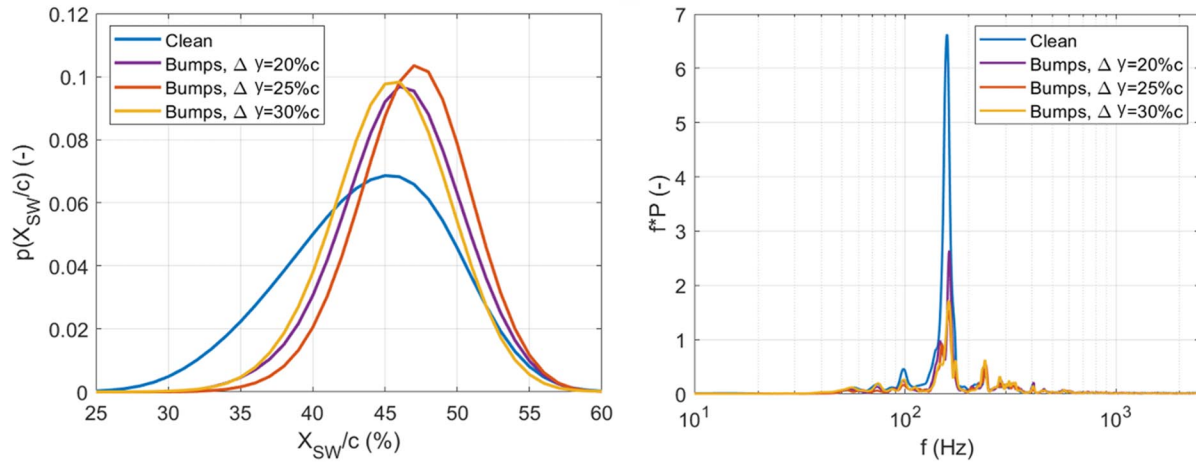


Fig. 8 Distribution (left) and spectrum (right) associated with shock position for configurations with and without SCBs.

To quantify the variation of the range of shock-wave oscillation, in Fig. 8 (left), the probability density function  $p(X_{SW}/c)$  of the shock position is shown for the clean as well as for the SCB configurations with different spacings. The result clearly illustrates that with any SCB configuration, a reduction of the oscillation range of the SW is obtained. Furthermore, the average shock position is slightly shifted toward more downstream positions. The best performance in terms of shock-wave oscillation reduction is obtained for a bump spacing of  $25\%c$ , whereas good performance is also achieved for the  $\Delta y_{SCB} = 27.5\%c$  and  $\Delta y_{SCB} = 30\%c$  spacings. These observations are confirmed by the average values of the shock position  $\bar{X}_{SW}$  and the relative standard deviation  $\sigma(X_{SW})$  reported in Table 4. The figures clarify that for  $\Delta y_{SCB} = 25\%c$ , the weakest fluctuations of the shock wave, but also the most downstream average shock position, occur.

The spectral content of the shock position signal is computed in the form of a power spectral density  $P(f)$  by using the Welch method and plotted in Fig. 8 (right) [as a premultiplied spectrum  $f \cdot P(f)$  for the clean configuration and for the airfoil in presence of bumps] with spacings of 20, 25, and  $30\%c$ . The image reveals that the buffet characteristic frequency is not affected by the use of SCBs, with all the configurations having a main peak at 160 Hz, which is in good agreement in terms of the Strouhal number ( $St = 0.07$ ) with Jacquin

et al. [3]. All the SCB configurations achieve a relevant reduction of the main peak of  $f \cdot P$ , although the most important reduction is obtained for  $\Delta y_{SCB} = 25\%c$ . The values of  $f \cdot P$  at 160 Hz are summarized in Table 4 for all the tested configurations.

Tracking the shock position from PIV data, similar results are obtained with a reduction of more than 50% of the main peak at 160 Hz when the SCBs are used and with a slight optimization for the  $\Delta y_{SCB} = 25\%c$  configuration. For brevity, these results are not included.

## IV. Flowfield Analysis

### A. Buffet Cycle Dynamics

To gain further insight on the effect of 3-D SCBs on the buffet cycle, PIV instantaneous images are shown in Figs. 9 and 10 for the  $\Delta y_{SCB} = 25\%c$  configuration, for two particular stages of the buffet cycle, corresponding to the most upstream and the most downstream positions of the shock oscillation. Both flowfields show the presence of a separated area, for which the extent is significantly smaller than the region present in Fig. 6 (left). Similar to the behavior of transonic buffet on a clean airfoil (in absence of control systems) [3,36], also in presence of SCBs the variation of the separated area through the buffet cycle is such, that it reaches its maximum extent during the upstream travel of the SW (see Fig. 6) and its lowest extent during its downstream travel (not explicitly shown here).

The snapshot in Fig. 9 (left) shows the velocity field in the most upstream position with the moving shock wave located slightly upstream ( $41\%c$ ) of the crest of the SCB. Figure 9 (right) visualizes the corresponding instantaneous spanwise organization of the velocity field. Note that this snapshot was not acquired simultaneously with the one in Fig. 9 (left), using the data on the vertical airfoil; yet, it has been selected to correspond to the same phase in the buffet cycle. This visualization clarifies that the oblique shock waves that originate at the leading edge of the SCBs curve around the bumps, with the SW structures eventually interacting with each other. Downstream of this

Table 4 Comparison of shock position properties for all the tested configurations from schlieren data

Configuration	$\bar{X}_{SW}, \%c$	$\sigma(X_{SW}), \%c$	$f \cdot P(f = 160 \text{ Hz})$
Clean	43.8	5.3	6.6
$\Delta y_{SCB} = 20\%c$	46.1	3.7	2.7
$\Delta y_{SCB} = 22.5\%c$	45.5	3.9	3.0
$\Delta y_{SCB} = 25\%c$	47.0	3.3	1.5
$\Delta y_{SCB} = 27.5\%c$	45.9	3.4	2.0
$\Delta y_{SCB} = 30\%c$	45.4	3.6	1.7

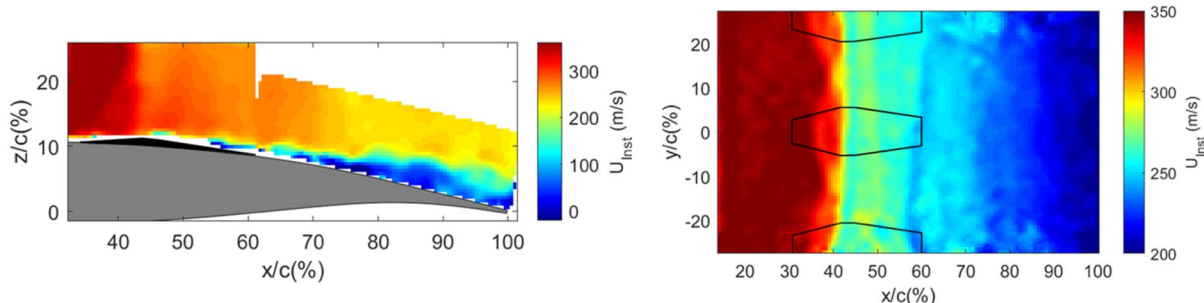
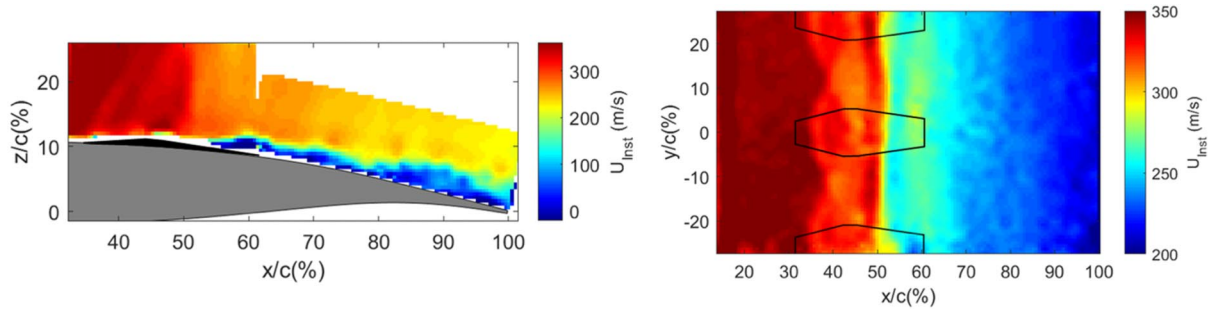


Fig. 9 Uncorrelated instantaneous horizontal velocity fields in presence of SCBs ( $\Delta y_{SCB} = 25\%c$ ) with SW in its most upstream position: velocity field in chordwise-vertical plane (left), and another snapshot displayed in chordwise-spanwise plane together with outline of bumps (right).



**Fig. 10** Uncorrelated instantaneous horizontal velocity fields in presence of SCBs ( $\Delta y_{SCB} = 25\%c$ ) with SW in its most downstream position: velocity field in chordwise-vertical plane (left), and another snapshot in the chordwise-spanwise plane together with outline of bumps (right).

feature, the quasi-normal unsteady shock wave displays a very coherent distribution along the span of the airfoil.

Figure 10 (left) shows the instantaneous velocity field with the quasi-normal SW in proximity of the most downstream position (close to  $50\%c$ ) and with the separated area extent again quite limited. By looking at the chordwise-spanwise distribution of the velocity, the presence of the different curved steady shock waves originating at the leading edge of the bumps is still evident. The supersonic area is terminated again with a 2-D quasi-normal shock wave at  $x/c \approx 50\%$ .

Despite this observed spanwise coherence, the separated area is not expected to be 2-D, as suggested by the oil flow visualization in Fig. 1 (left). This information cannot be extracted from the PIV data from the vertical airfoil because the measurement plane was detached from the surface of the airfoil and located just above the separated area region (see Fig. 4, right).

### B. Main Statistics of the Velocity Field

The first quantitative description of the velocity field is provided by the distribution of the average horizontal velocity component for both the clean airfoil and the airfoil in the presence of the best-performing SCB configuration, i.e. with  $\Delta y_{SCB} = 25\%c$  (Fig. 11). Although the average flowfield is not representative of a specific flow condition, it allows the observation and comparison of the relevant flow structures of both configurations. For the uncontrolled airfoil, the mean SW location is not easily identifiable because of the SW oscillation, which results in a gradual compression rather than a sharp interface. In contrast, in the presence of control devices, an oblique SW at the leading edge of the SCB is clearly distinguished. From this comparison, no important difference is noticed in terms of the extent

of the separated area; however, a wider shear layer (approximated by the green/yellow area in the velocity field) seems to be present for the clean airfoil.

Streamlines are included in the velocity field with their general behavior being very similar for the two configurations. As expected, for the SCB configuration, a variation of the inclination of the streamlines is noticeable in correspondence with the oblique shock wave.

To highlight the unsteadiness present in the flowfield, Fig. 12 shows the standard deviation of the horizontal velocity component for the same configurations shown in Fig. 11. In terms of the SW position, the results are in good agreement with those presented in the previous section, with a smaller range of oscillation of the SW for the controlled case. These ranges are in accordance with those shown in Fig. 8 (left), and they furthermore confirm the stabilizing effect obtained with the  $\lambda$  shape of the SW. In proximity of  $z/c = 25\%$  and  $x/c = 45\%$ , there is an increase of the standard deviation values for the SCB configuration. This growth is associated with the moving shock wave also traveling (at that location) upstream of the steady oblique shock wave when reaching its most upstream position. The distribution of the standard deviation downstream of the shock wave confirms a reduction of the fluctuation of both the separated area and of the shear layer in the presence of SCBs.

### C. Separated Area Behavior

A first view of the separated area and shear layer structure is provided in Fig. 13 by the profiles of the horizontal velocity component for three different chordwise positions:  $x/c = 60\%$ ,  $x/c = 80\%$ , and  $x/c = 100\%$ . The data are here shown for the clean, the

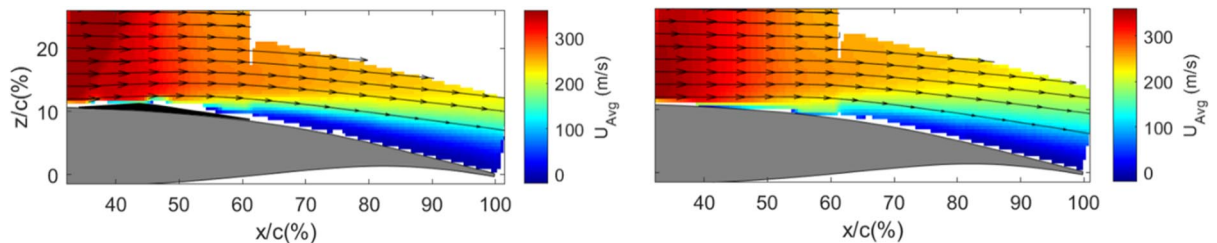


**Fig. 11** Average horizontal velocity component for the airfoil in the presence of SCBs with  $\Delta y_{SCB} = 25\%c$  (left) and for the clean configuration (right).

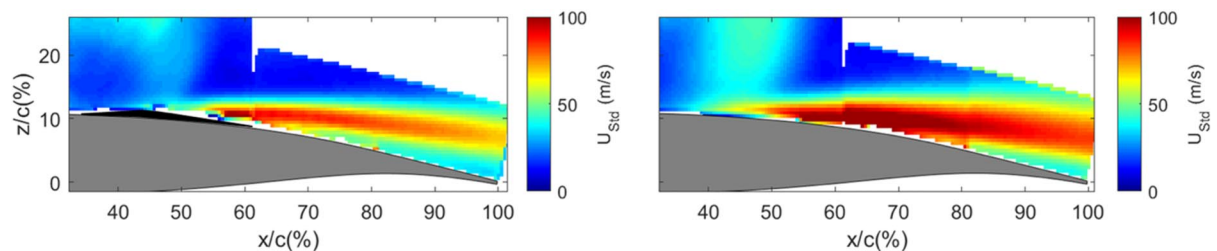


**Fig. 12** Standard deviation of the horizontal velocity component for the airfoil in the presence of SCBs with  $\Delta y_{SCB} = 25\%c$  (left) and for the clean configuration (right).



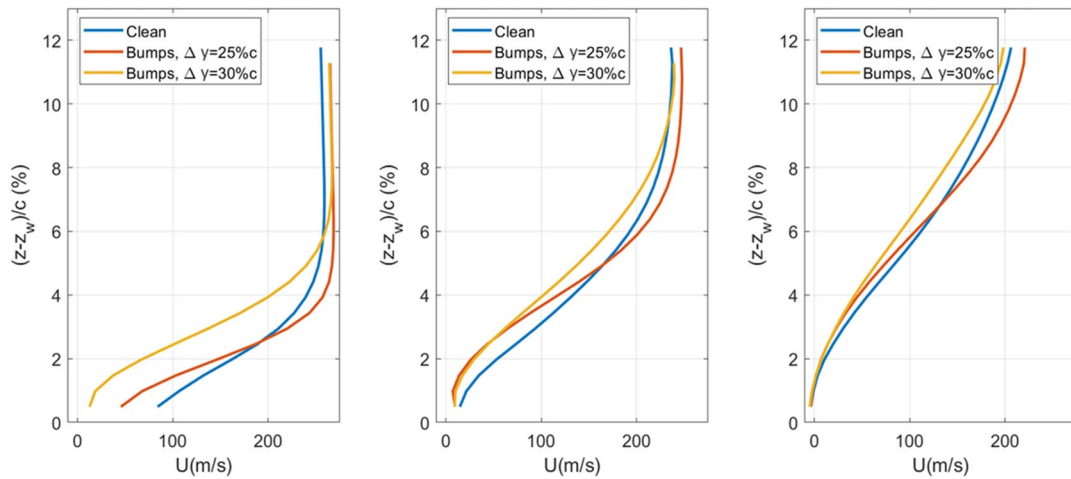


Fig. 13 Horizontal velocity profile at  $x/c = 60\%$  (left),  $x/c = 80\%$  (center), and  $x/c = 100\%$  (right) for the three configurations tested.

$\Delta y_{SCB} = 25\%c$ , and the  $\Delta y_{SCB} = 30\%c$  configurations. All the velocity profiles are shown with respect to the local height of the airfoil surface  $z_w(x/c)$ ; therefore, the vertical axis always indicates the local distance from the surface of the airfoil:  $(z - z_w)/c$ . It is observed that the  $\Delta y_{SCB} = 25\%c$  profiles are all on the left of the profiles for the clean case in proximity of the surface of the airfoil (in the separated area) and on the right above the inflection points of the former. The shape of the profile suggests a thinning of the shear layer for the SCB configuration with a spacing of  $25\%c$ . On the contrary, this effect is not observed for the second spacing tested ( $\Delta y_{SCB} = 30\%c$ ), with its profile almost overlapping the profile of the clean configuration for  $(z - z_w(x/c))/c > 10\%$ . When comparing the behavior of the two bump configurations, lower values of horizontal velocity are observed for the  $30\%c$  configuration, suggesting the presence of higher-momentum losses for this case.

In Fig. 14, the profiles of the standard deviation of the horizontal velocity component are shown for the same chordwise locations and configurations. The graphs clarify that, with a spacing of  $25\%c$ , the fluctuations in the separated area are always reduced when compared to the clean configuration. On the other hand,  $\Delta y_{SCB} = 30\%c$  displays a reduction of the fluctuations at  $x/c = 80\%$  and  $x/c = 100\%$  but an increase just downstream of the SW oscillating range for  $x/c = 60\%$ .

The reduced values of the standard deviation for the  $25\%c$  configuration are observed in the full region analyzed [except for a restricted region for  $z - z_w(x/c = 0.6) > 10\%c$ ] and are expected to be associated with the reduced shock-wave oscillations. What stands out is that, for the clean configuration, the standard deviation of the velocity near the airfoil surface is much higher than for the SCB configurations. This increase in standard deviation could be attrib-

uted to the fact that for the clean configuration, there is an established oscillation between stages in which the flow is fully attached and stages in which the shock foot separation is triggered (for an understanding of the separated area behavior for the clean configuration, see the phase-averaged analysis of D'Aguanno et al. [36]). For the bump configurations, on the other hand, the velocity at  $60\%$  of the chord is highly influenced by the proximity of the bump, which in view of the tail vortices present is expected to reduce the occurrence of intermittent shock foot separation, and thus is expected to decrease the standard deviation values relative to the streamwise velocity component.

To quantitatively analyze the extent of the separated area, the probability of separated flow is evaluated by showing the percentage of vectors with a negative streamwise velocity (reverse flow) with an approach similar to that of Giepmans et al. [40]. The results of this analysis are plotted in Fig. 15 (left) for the  $\Delta y_{SCB} = 25\%c$  (top) and the clean (bottom) configurations. The plot suggests that there is quite a similar probability of having separated flow close to the surface of the airfoil. However, for the SCB configuration, there is a slightly increased probability of having separated flow for  $65\% < x/c < 77\%$  (immediately downstream of the SCB). Notwithstanding the previous consideration, in the remaining FOV, the region of the flow in which reverse flow is likely to be present is wider for the clean configuration, confirming a beneficial effect of using SCBs for reducing the extent of the separated area. This is well visualized in Fig. 15 (right), where the profile of  $P_{Sep}$  is shown for both the clean and the SCB configurations, for  $x/c = 80\%$  and  $x/c = 100\%$ . In both cases, a clear reduction of probability of separation is observed in the presence of the control system. The probability of the separated area plot is spatially integrated to compute the extent of the reverse

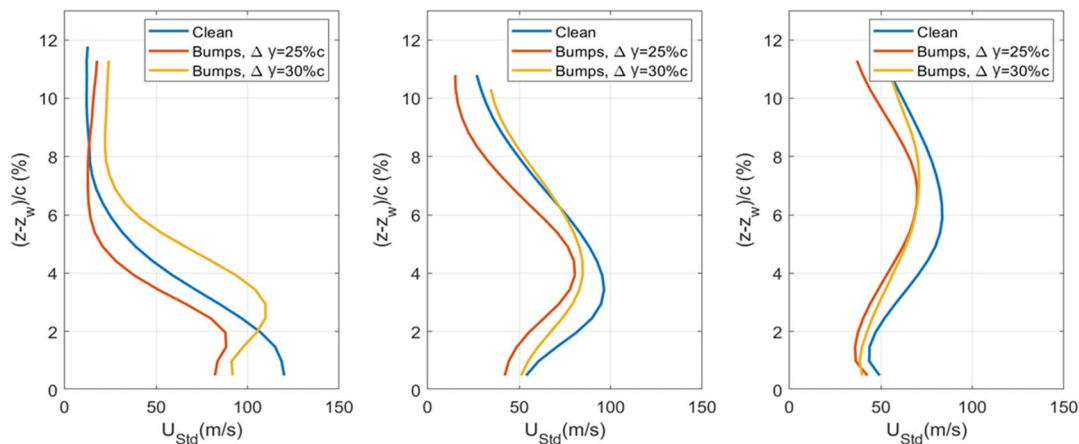
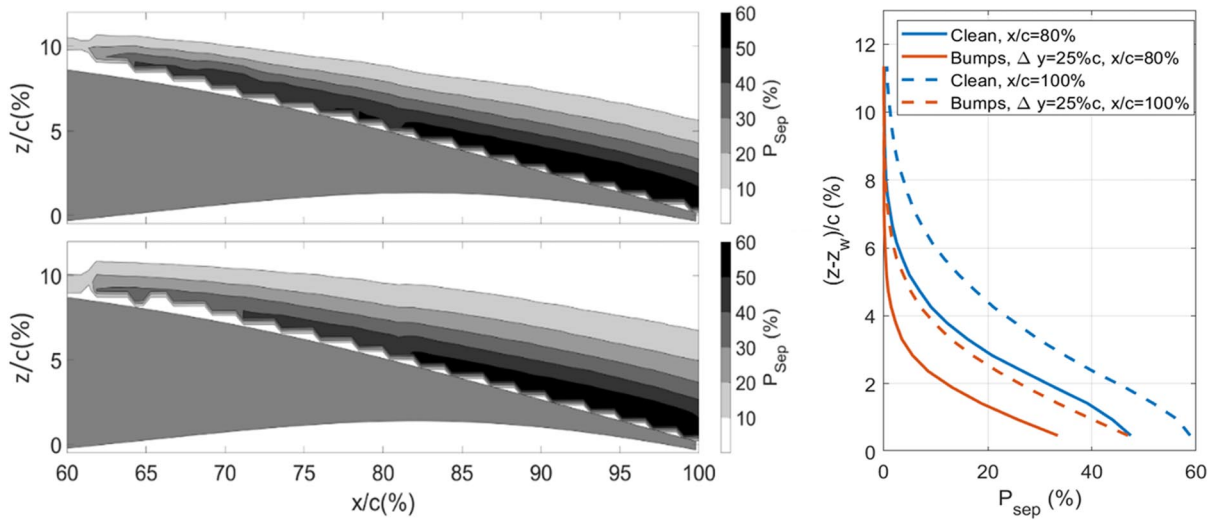


Fig. 14 Profile of standard deviation of horizontal velocity component at  $x/c = 60\%$  (left),  $x/c = 80\%$  (center), and  $x/c = 100\%$  (right) for the three configurations tested.



**Fig. 15** On the left: probability of reverse flow ( $U < 0$ ) for airfoil in the presence of SCBs with  $\Delta y_{\text{SCB}} = 25\%c$  (top) and for clean airfoil (bottom). On the right: relative profile for  $x/c = 80\%$  and  $x/c = 100\%$ .

**Table 5** Separated area extent per configuration

Parameter	Clean	$\Delta y_{\text{SCB}} = 25\%c$	$\Delta y_{\text{SCB}} = 30\%c$
$A_{\text{Sep}}, \%$	15	13	17
$\sigma(A_{\text{Sep}}), \%$	19	13	18

flow region  $A_{\text{Sep}}$ . These data have been summarized in Table 5, which reveals a reduction of the separated area for the  $\Delta y_{\text{SCB}} = 25\%c$  configuration as compared to the clean case.

The reduction in the reverse flow area for the  $\Delta y_{\text{SCB}} = 25\%c$  case could be a result of the vortical structures developing from the tail of the bumps (accurately described by Ogawa et al. [18] and Collissi et al. [22]). Furthermore, for the SCB case, the simultaneous presence of an oblique shock wave and a quasi-normal shock wave is less dissipative as compared to the single shock-wave structure present for the clean configuration, and hence a reduction of the adverse pressure ratio could have been expected.

In addition to the calculation of the average extent of the reverse flow area, the extent of this region has been computed in each instantaneous snapshot. From the time evolution of the extent of the separated region, the relative standard deviation is obtained [see  $\sigma(A_{\text{Sep}})$  in Table 5]. The values highlight that the extent of the reverse flow area is fluctuating in time more intensely for the clean configuration than for the  $\Delta y_{\text{SCB}} = 25\%c$  case, which is in good agreement with Fig. 12, where the standard deviation of the horizontal velocity field showed a decrease of the fluctuations in the separated area. These procedures have also been applied to  $\Delta y_{\text{SCB}} = 30\%c$ , although the relative reverse flow probability plot has not been included for brevity. For this configuration, the average separated area is larger than for the other two configurations; however, a slight decrease of the pulsation of the separated area is observed as compared to the clean configuration.

From the time behavior of the extent of the reverse flow region, the relative spectral content has been derived in the form of a premultiplied power spectral density (Fig. 16). This reveals that the dominant frequency is the same as for the shock-wave oscillation (160 Hz). The amplitude of this main peak is once again reduced in presence of SCBs, and the performance is optimized for  $\Delta y_{\text{SCB}} = 25\%c$ . This reduction is very similar to the decrease observed for the shock position in Fig. 8, confirming that the SW oscillation and the pulsation of the separated area are closely related (as also shown by D'Aguanno et al. [36] and Grossi et al. [41]). Although not directly shown in this paper, a further PIV spectral analysis has confirmed that all the regions of high-velocity fluctuations in the entire FOV (for all the investigated configurations) are dominated by contributions at the buffet frequency (160 Hz).

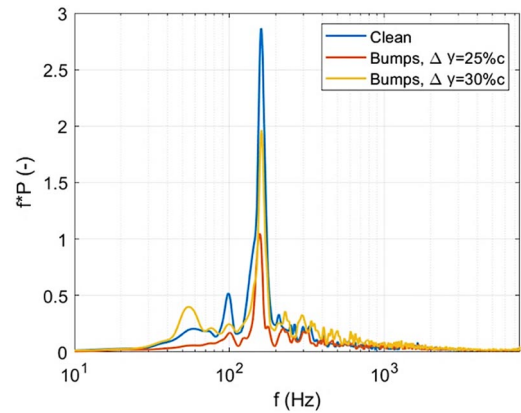


**Fig. 16** Spectral analysis of reverse flow area for the different configurations.

#### D. Effect of SCB Spacing on the Average Flowfield

To better understand the difference in behavior between the bump configurations with spacings of  $\Delta y_{\text{SCB}} = 25\%c$  and  $\Delta y_{\text{SCB}} = 30\%c$ , the corresponding average velocity fields in the spanwise–chordwise plane are shown in Fig. 17 (similar data for the clean configuration can be found in the work of D'Aguanno et al. [5]). The spanwise structure of the shock wave is once again highlighted, with the presence of both a curved SW originating from the leading edge of the bumps and the quasi-normal SW, which is located close to the crest of the bumps.

For geometric reasons, the curved shock waves developing around neighboring bumps interact with each other at a distance  $\Delta y_{\text{SCB}}/2$  from the symmetry planes of the bumps. Figure 17 clarifies that the curved shock waves are still present after interacting with each other: interacting one more time in correspondence with the symmetry plane of the different bumps. It is clear that the chord position of this second interaction depends strongly on the spacing  $\Delta y_{\text{SCB}}$ , with it happening more downstream for the wider spacing. Therefore, in the case of the smaller spacing ( $\Delta y_{\text{SCB}} = 25\%c$ ), curved shock waves are not present beyond  $x/c = 45\%$ . In contrast, for  $\Delta y_{\text{SCB}} = 30\%c$ , the presence of the curved SW is observed until the most downstream position of the quasi-normal shock wave ( $x/c = 50\%$ ).

This difference results in a non-negligible dissimilarity in the velocity field for  $35\% < x/c < 50\%$ . Consequently, the effect of this interaction is assumed to have an influence on the buffet oscillations and on the 2-D coherence of the flowfield. This observation is in agreement with the works of Ogawa et al. [18] and Bruce and Babinsky [20], in which it was stated that (although for flow conditions different than

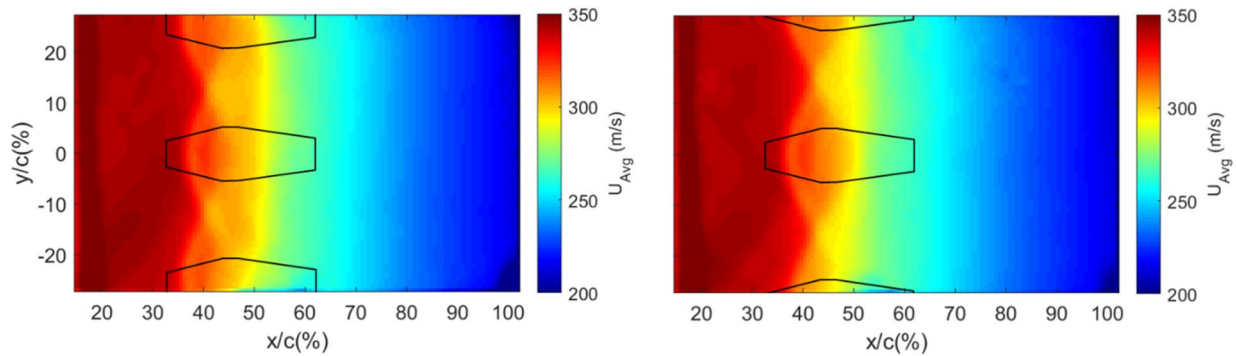


Fig. 17 Average horizontal velocity field in the spanwise–chordwise plane in the presence of SCBs with  $\Delta y_{SCB} = 25\%c$  (left) and with  $\Delta y_{SCB} = 30\%c$  (right). In both cases, the outlines of the bumps are specified.

those discussed in this study) properly spaced 3-D SCBs can induce a favorable quasi-2-D SW along the full span.

To better substantiate the differences in the velocity field along the span of the airfoil, profiles of the horizontal velocity component are plotted in Fig. 18 for four different chordwise locations: 30, 40, 50, and 60%. In addition to the two SCB configurations, the clean configuration is added for reference. Slightly upstream of the leading edge of the SCBs ( $x/c = 30\%$ ), the three velocity profiles are, as expected, very similar.

At 40% of the chord, the velocity is higher for the clean configuration than for the other two configurations because in most of the snapshots, the flow is still supersonic (average shock-wave location at about 45%c); whereas for the SCBs configurations, the horizontal velocity is affected by the upstream oblique (curved) shock wave. Close to the centerline of the airfoil ( $-0.08 < y/c < 0.08$ ), similar velocity profiles are visualized for the two SCB configurations; whereas at more outboard locations, the velocity profiles are highly influenced by the different spacing. The fact that adjacent curved shock waves interact at more outboard spanwise locations for the wider spacing also affects the chordwise location of this interaction (taking place about 5% more downstream for  $\Delta y_{SCB} = 30\%c$ ), as confirmed by the behavior of the profiles.

At 50%c, all velocity distributions are relatively uniform but with lower-velocity values for the clean configuration than for the two SCB configurations, due to the presence of the single quasi-normal shock wave for this configuration. When comparing the two SCB configurations mutually, lower-velocity values are observed for the configuration with the wider bump spacing, which could possibly be caused by a more dissipative secondary shock-wave structure. Further downstream at  $x = 60\%$ , which is in proximity of the trailing edge of the bumps, the differences between the three velocity

profiles have become even smaller, with lower velocities for the clean configuration and slightly higher velocities for the 25%c configuration, similar to at the previous station.

To emphasize the spanwise behavior of the flowfield, the average of the spanwise velocity component is shown in Fig. 19 for the two SCB configurations, highlighting nonnegligible differences. The velocity fields are here plotted for  $30\% < x/c < 100\%$  and for  $-16\% < y/c < 16\%$ , indicating the symmetry planes between adjacent bumps with dashed lines. First of all, in the region enclosed between the leading-edge curved shock wave of a given bump and the curved shock wave originating from an adjacent bump, a spanwise deflection of the flow away from the bump is observed. Because, for the wider spacing case, the curved shock waves interact with each other at a further spanwise location, the region of high (absolute) spanwise velocity is consequently wider as well.

Other relevant differences are observable in correspondence with the side flanks of the bumps. For the  $\Delta y_{SCB} = 25\%c$  spacing, the signature of a streamwise vortex pair is observable downstream of the crest of the bump, which is recognizable because of the two regions of spanwise flow toward the centerline of the bump occurring at the opposite bump sides. The formation of this vortex pair in on-design conditions has been documented in detail by both Bruce and Colliss [17] and Colliss et al. [22]. As was reported there, the presence of this vortex pair induces a downwash region in the bump wake, which assists in energizing the flow with a beneficial effect on the suppression of the separated area. Similar structures are not observable in the PIV data in Fig. 19 (right) for the  $\Delta y_{SCB} = 30\%c$  configuration (at least not in this detached measurement plane), for which there is only a small region of negative spanwise velocity in correspondence with the tail of the SCB. This difference in behavior for  $\Delta y_{SCB} = 30\%c$  could possibly be caused by the reduced strength of the streamwise

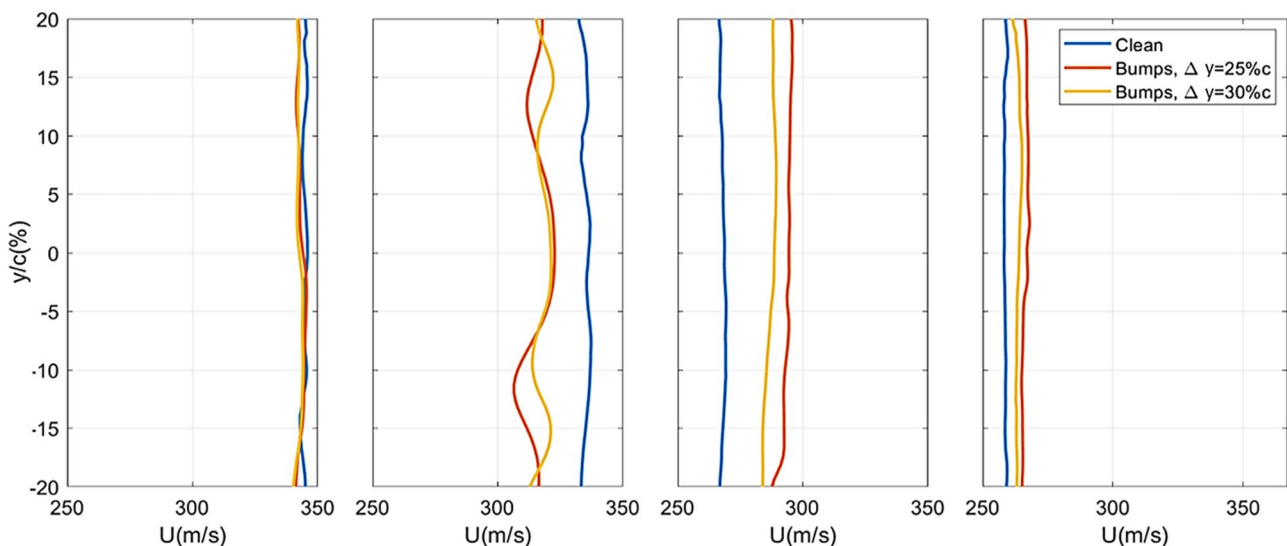
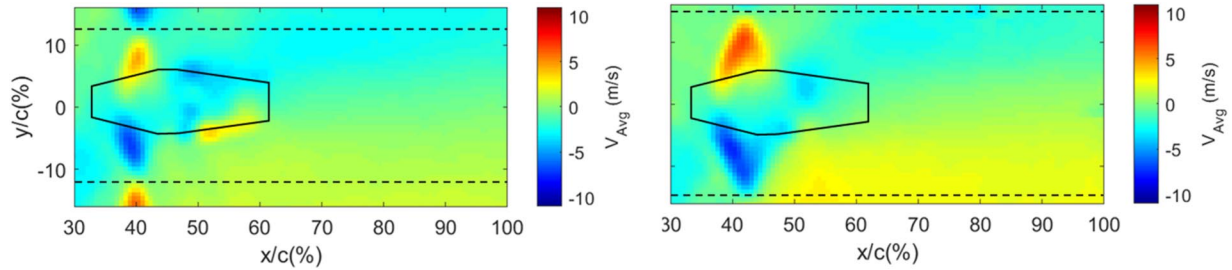
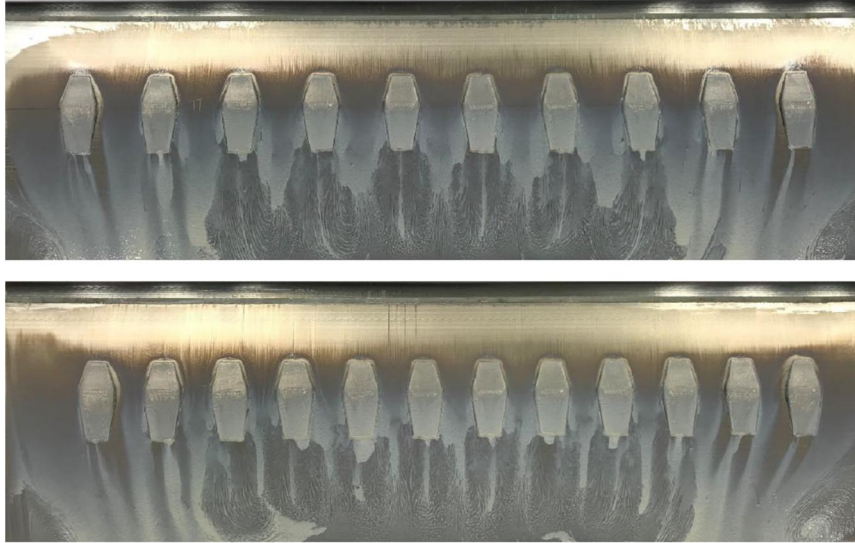


Fig. 18 Horizontal velocity profile along the span at  $x/c = 30, 40, 50, 60\%$  (from left to right) for the three configurations tested.





**Fig. 19** Average vertical velocity field in the spanwise–chordwise plane in the presence of SCBs with  $\Delta y_{SCB} = 25\%c$  (left) and with  $\Delta y_{SCB} = 30\%c$  (right). In both cases, the outline of the bumps is specified.



**Fig. 20** Comparison of oil flow visualizations for  $\Delta y_{SCB} = 25\%c$  (top) and  $\Delta y_{SCB} = 20\%c$  (bottom) configurations.

vortex pair by the flow being already separated downstream of the crest of the bumps.

Although the oil flow visualization is not available for the  $\Delta y_{SCB} = 30\%c$  case, in Fig. 20, the oil flow of the  $\Delta y_{SCB} = 25\%c$  case is compared to the visualization relative to the  $\Delta y_{SCB} = 20\%c$  configuration to show dependence of these vortical structures on the spacing parameter. For both the configurations, corner effects influence the production of the vortical structures from the tail of the two most external SCBs (at both the extremities of the model), whereas no influence is observed for the “internal” SCBs. For both of the SCB configurations, counter-rotating vortices develop specularly with respect to the symmetry plane of each SCB. For the  $\Delta y_{SCB} = 20\%c$  configuration (Fig. 20, bottom), the vortical structures originating from the tails of adjacent SCBs interact at a more upstream chordwise location ( $x \approx 65\%c$ ) when compared to the  $\Delta y_{SCB} = 25\%c$  configuration ( $x \approx 75\%c$ ). An opposite behavior, with a more downstream interaction of contiguous vortical structures, is expected for the  $\Delta y_{SCB} = 30\%c$  case.

These visualizations provide further hints that the distance between the SCBs directly influences the behavior of the separated area by changing the character of the SCB vortical structures. To reduce the possible detrimental behavior of SCBs in off-design conditions (although very limited as compared to 2-D SCBs [30]), an adaptive implementation of these devices on future vehicles is suggested [42–44].

## V. Conclusions

The results of this study confirm that 3-D SCBs are suitable devices for controlling transonic buffet. It is shown that these control devices reduce the shock oscillation while changing the structure of the shock wave into a  $\lambda$  shape. From a spectral point of view, the use of these devices does not affect the buffet frequency ( $f = 160$  Hz) but

clearly attenuates the contribution of the main peak. An optimization of the performance (in reducing buffet) results when a spanwise array of bumps with a spacing of  $25\%c$  is adopted, with a reduction of the standard deviation of the shock position (compared to the clean configuration) of 37% when computed from schlieren data and 34% from PIV data.

In addition to the stabilization of the shock position, a diminished pulsation of the separated area is achieved with the application of SCBs. The comparison of the separated regions of the different configurations highlights a relevant influence of the spacing parameter, with the results clearly optimized for a spacing of  $\Delta y_{SCB} = 25\%c$ , for which even a reduction of 14% of the average extent of the separated area is achieved when compared to the clean configuration. This reduction also gives hints that, in the presence of the best-behaving SCB configuration ( $\Delta y_{SCB} = 25\%c$ ), drag is not negatively affected.

To further investigate the difference in behavior among the various SCB configurations, PIV flow visualization in a spanwise–chordwise-oriented plane was performed. This proved to be particularly meaningful for the understanding of the mutual interaction between the different bumps and the effect of changing their spacing on the relevant flow structures. It is shown that the oblique shock waves, originating at the leading edge of the three-dimensional SCBs, curve around the bumps (Fig. 17). The velocity data have furthermore confirmed the presence of counter-rotating vortex structures, developing from the tail of the bumps, which are well identified only for the  $25\%c$  SCB configuration. This vortex production is also qualitatively observed in an oil flow visualization. These PIV results also allowed assessment of the two-dimensionality of the flowfield. The velocity fields exhibited a spanwise coherence of the quasi-normal moving shock wave for the  $\Delta y_{SCB} = 25\%c$  configuration, notwithstanding the presence of the three-dimensionality of the control system. Additional three-dimensional SW structures arose for a wider spacing of the bumps.



The similarity of the results for the shock-wave detection obtained with schlieren and PIV measurements confirms that schlieren visualizations can be effectively used for studying the shock-wave behavior on an airfoil, also in presence of three-dimensional bumps. However, additional relevant effects of the SCBs on the transonic buffet cycle cannot be observed with schlieren visualization. For example, the effect of different spacings was found to influence the separated area behavior (which cannot be quantified by the schlieren visualizations of this study) more prominently than the shock-wave behavior, for which the stabilization is achieved with all the SCBs configurations tested.

In conclusion, this study demonstrates the feasibility of controlling transonic buffet using 3-D SCBs, and it confirms the influence of the spacing parameter. When properly spaced, the SCBs were also demonstrated as being effective in both of their possible working principles: shock-wave stabilization, and reduction of the separated area extent.

### Acknowledgments

This work has been carried out as part of the Holistic Optical Metrology for Aero-Elastic Research project, which is funded by the European Commission, program H2020, under grant no. 769237. The authors acknowledge Manfredi Messina for assisting with the realization of the shock control bumps and setting up part of the experiments.

### References

- [1] Hilton, W. F., and Fowler, R. G., "Photographs of Shock Wave Movement," National Physical Lab. R&M 2692, England, U.K., 1947.
- [2] Lee, B. H. K., "Transonic Buffet on a Supercritical Airfoil," *Aeronautical Journal*, Vol. 94, No. 935, 1990, pp. 143–152. <https://doi.org/10.1017/S0001924000022752>
- [3] Jacquin, L., Molton, P., Deck, S., Maury, B., and Soulevant, D., "Experimental Study of Shock Oscillation over a Transonic Supercritical Profile," *AIAA Journal*, Vol. 47, No. 9, 2009, pp. 1985–1994. <https://doi.org/10.2514/1.30190>
- [4] Hartmann, A., Feldhusen, A., and Schröder, W., "On the Interaction of Shock Waves and Sound Waves in Transonic Buffet Flow," *Physics of Fluids*, Vol. 25, No. 2, 2013, Paper 026101. <https://doi.org/10.1063/1.4791603>
- [5] D'Agunno, A., Schrijer, F. F. J., and van Oudheusden, B. W., "Spanwise Organization of Upstream Traveling Waves in Transonic Buffet," *Physics of Fluids*, Vol. 33, No. 10, 2021, Paper 106105. <https://doi.org/10.1063/5.0062729>
- [6] Crouch, J. D., Garbaruk, A., Magidov, D., and Travin, A., "Origin of Transonic Buffet on Aerofoils," *Journal of Fluid Mechanics*, Vol. 628, June 2009, pp. 357–369. <https://doi.org/10.1017/S0022112009006673>
- [7] Sartor, F., Mettot, C., and Sipp, D., "Stability, Receptivity, and Sensitivity Analyses of Buffeting Transonic Flow over a Profile," *AIAA Journal*, Vol. 53, No. 7, 2015, pp. 1980–1993. <https://doi.org/10.2514/1.J053588>
- [8] Giannelis, N. F., Vio, G. A., and Levinski, O., "A Review of Recent Developments in the Understanding of Transonic Shock Buffet," *Progress in Aerospace Sciences*, Vol. 92, July 2017, pp. 39–84. <https://doi.org/10.1016/j.paerosci.2017.05.004>
- [9] Caruana, D., Mignosi, A., Robitaille, C., and Corrège, M., "Separated Flow and Buffeting Control," *Flow, Turbulence and Combustion*, Vol. 71, No. 1, 2003, pp. 221–245. <https://doi.org/10.1023/B:APPL.0000014918.93432.4f>
- [10] Caruana, D., Mignosi, A., Corrège, M., Le Pourhiet, A., and Rodde, A. M., "Buffet and Buffeting Control in Transonic Flow," *Aerospace Science and Technology*, Vol. 9, No. 7, 2005, pp. 605–616. <https://doi.org/10.1016/j.ast.2004.12.005>
- [11] Ren, K., Chen, Y., Gao, C., and Zhang, W., "Adaptive Control of Transonic Buffet Flows over an Airfoil," *Physics of Fluids*, Vol. 32, No. 9, 2020, Paper 096106. <https://doi.org/10.1063/5.0020496>
- [12] Lee, B. H. K., "Effects of Trailing-Edge Flap on Buffet Characteristics of a Supercritical Airfoil," *Journal of Aircraft*, Vol. 29, No. 1, 1992, pp. 93–100. <https://doi.org/10.2514/3.46130>
- [13] Despre, C., Caruana, D., Mignosi, A., Reberga, O., and Corrège, M., "Buffet Active Control—Experimental and Numerical Results," *Proceedings of the RTO AVT Symposium on Active Control Technology of Enhanced Performance Operational Capabilities of Military Aircraft, Land Vehicles, and Sea Vehicles, MP-051*, June 2001.
- [14] Tian, Y., Li, Z., and Liu, P. Q., "Upper Trailing-Edge Flap for Transonic Buffet Control," *Journal of Aircraft*, Vol. 55, No. 1, 2018, pp. 382–389. <https://doi.org/10.2514/1.C033134>
- [15] D'Agunno, A., Schrijer, F. F. J., and van Oudheusden, B. W., "Experimental Characterization of Upper Trailing Edge Flaps for Transonic Buffet Control," *Flow, Turbulence and Combustion*, Vol. 110, No. 2, 2022, pp. 325–350. <https://doi.org/10.1007/s10494-022-00381-3>
- [16] Brion, V., Dandois, J., Mayer, R., Reijasse, P., Lutz, T., and Jacquin, L., "Laminar Buffet and Flow Control," *Proceedings of the Institution of Mechanical Engineers, Part G: Journal of Aerospace Engineering*, Vol. 234, No. 1, 2019, pp. 124–139. <https://doi.org/10.1177/0954410018824516>
- [17] Bruce, P. J. K., and Colliss, S. P., "Review of Research into Shock Control Bumps," *Shock Waves*, Vol. 25, No. 5, 2015, pp. 451–471. <https://doi.org/10.1007/s00193-014-0533-4>
- [18] Ogawa, H., Babinsky, H., Pätzold, M., and Lutz, T., "Shock-Wave/Boundary-Layer Interaction Control Using Three-Dimensional Bumps for Transonic Wings," *AIAA Journal*, Vol. 46, No. 6, 2008, pp. 1442–1452. <https://doi.org/10.2514/1.32049>
- [19] Holden, H., and Babinsky, H., "Shock/Boundary Layer Interaction Control Using 3D Devices," *41st Aerospace Sciences Meeting and Exhibit*, AIAA Paper 2003-0447, 2003. <https://doi.org/10.2514/6.2003-447>
- [20] Bruce, P. J. K., and Babinsky, H., "Experimental Study into the Flow Physics of Three-Dimensional Shock Control Bumps," *Journal of Aircraft*, Vol. 49, No. 5, 2012, pp. 1222–1233. <https://doi.org/10.2514/1.C031341>
- [21] Babinsky, H., and Ogawa, H., "SBLI Control for Wings and Inlets," *Shock Waves*, Vol. 18, June 2008, pp. 89–96. <https://doi.org/10.1007/s00193-008-0149-7>
- [22] Colliss, S. P., Babinsky, H., Nübler, K., and Lutz, T., "Vortical Structures on Three-Dimensional Shock Control Bumps," *AIAA Journal*, Vol. 54, No. 8, 2016, pp. 2338–2350. <https://doi.org/10.2514/1.J054669>
- [23] Zhang, Y., Yang, P., Li, R., and Chen, H., "Unsteady Simulation of Transonic Buffet of a Supercritical Airfoil with Shock Control Bump," *Aerospace*, Vol. 8, No. 8, 2021, Paper 203. <https://doi.org/10.3390/aerospace8080203>
- [24] Colliss, S. P., Babinsky, H., Nübler, K., and Lutz, T., "Joint Experimental and Numerical Approach to Three-Dimensional Shock Control Bump Research," *AIAA Journal*, Vol. 52, No. 2, 2014, pp. 436–446. <https://doi.org/10.2514/1.J052582>
- [25] Mayer, R., Lutz, T., and Krämer, E., "Numerical Study on the Ability of Shock Control Bumps for Buffet Control," *AIAA Journal*, Vol. 56, No. 5, 2018, pp. 1978–1987. <https://doi.org/10.2514/1.J056737>
- [26] Deng, F., and Qin, N., "Vortex-Generating Shock Control Bumps for Robust Drag Reduction at Transonic Speeds," *AIAA Journal*, Vol. 59, No. 10, 2021, pp. 3900–3909. <https://doi.org/10.2514/1.J060528>
- [27] Jones, N. R., Eastwood, J. P., and Jarrett, J. P., "Adapting Three-Dimensional Shock Control Bumps for Swept Flows," *AIAA Journal*, Vol. 55, No. 3, 2017, pp. 861–873. <https://doi.org/10.2514/1.J055169>
- [28] Eastwood, J. P., and Jarrett, J. P., "Toward Designing with Three-Dimensional Bumps for Lift/Drag Improvement and Buffet Alleviation," *AIAA Journal*, Vol. 50, No. 12, 2012, pp. 2882–2898. <https://doi.org/10.2514/1.J051740>
- [29] Tian, Y., Gao, S. Q., Liu, P. Q., and Wang, J. J., "Transonic Buffet Control Research with Two Types of Shock Control Bump Based on RAE2822 Airfoil," *Chinese Journal of Aeronautics*, Vol. 30, No. 5, 2017, pp. 1681–1696. <https://doi.org/10.1016/j.cja.2017.07.011>
- [30] Mayer, R., Lutz, T., Krämer, E., and Dandois, J., "Control of Transonic Buffet by Shock Control Bumps on Wing-Body Configuration," *Journal of Aircraft*, Vol. 56, No. 2, 2019, pp. 556–568. <https://doi.org/10.2514/1.C034969>
- [31] Paladini, E., Dandois, J., Sipp, D., and Robinet, J., "Analysis and Comparison of Transonic Buffet Phenomenon over Several Three-Dimensional Wings," *AIAA Journal*, Vol. 57, No. 5, 2018, pp. 1–18. <https://doi.org/10.2514/1.J056473>

- [32] Birkemeyer, J., Rosemann, H., and Stanewsky, E., "Shock Control on a Swept Wing," *Aerospace Science and Technology*, Vol. 4, No. 5, 2000, pp. 147–156.  
[https://doi.org/10.1016/S1270-9638\(00\)00128-0](https://doi.org/10.1016/S1270-9638(00)00128-0)
- [33] Bogdanski, S., Nübler, K., Lutz, T., and Kramer, E., "Numerical Investigation of the Influence of Shock Control Bumps on the Buffet Characteristics of a Transonic Airfoil," *New Results in Numerical and Experimental Fluid Mechanics IX*, Vol. 124, Springer, New York, 2014, pp. 23–32.  
[https://doi.org/10.1007/978-3-319-03158-3\\_3](https://doi.org/10.1007/978-3-319-03158-3_3)
- [34] Geoghegan, J. A., Giannelis, N. F., and Vio, G. A., "A Numerical Investigation of the Geometric Parametrisation of Shock Control Bumps for Transonic Shock Oscillation Control," *Fluids*, Vol. 5, No. 2, 2020, Paper 46.  
<https://doi.org/10.3390/fluids5020046>
- [35] König, B., Pätzold, M., Lutz, T., Krämer, E., Rosemann, H., Richter, K., and Uhlemann, H., "Numerical and Experimental Validation of Three Dimensional Shock Control Bumps," *Journal of Aircraft*, Vol. 46, No. 2, 2009, pp. 675–682.  
<https://doi.org/10.2514/1.41441>
- [36] D'Aguanno, A., Schrijer, F. F. J., and van Oudheusden, B. W., "Experimental Investigation of the Transonic Buffet Cycle on a Supercritical Airfoil," *Experiments in Fluids*, Vol. 62, Oct. 2021, pp. 1–23.  
<https://doi.org/10.1007/s00348-021-03319-z>
- [37] Sciacchitano, A., and Scarano, F., "Elimination of PIV Light Reflections via a Temporal High Pass Filter," *Measurement Science and Technology*, Vol. 25, No. 8, 2014, Paper 084009.  
<https://doi.org/10.1088/0957-0233/25/8/084009>
- [38] Humble, R. A., "Unsteady Flow Organization of a Shock Wave/ Boundary Layer Interaction," Ph.D. Thesis, Delft Univ. of Technology, Delft, The Netherlands, 2009.
- [39] Melling, A., "Tracer Particles and Seeding for Particle Image Velocimetry," *Experiments in Fluids*, Vol. 8, No. 12, 1997, pp. 1406–1416.  
<https://doi.org/10.1088/0957-0233/8/12/005>
- [40] Giepmans, R. H. M., Schrijer, F. F. J., and van Oudheusden, B. W., "A Parametric Study of Laminar and Transitional Oblique Shock Wave Reflections," *Journal of Fluid Mechanics*, Vol. 844, June 2018, pp. 187–215.  
<https://doi.org/10.1017/jfm.2018.165>
- [41] Grossi, F., Braza, M., and Hoarau, Y., "Prediction of Transonic Buffet by Delayed Detached-Eddy Simulation," *AIAA Journal*, Vol. 52, No. 10, 2014, pp. 2300–2312.  
<https://doi.org/10.2514/1.J052873>
- [42] Gramola, M., Bruce, P. J. K., and Santer, M., "Experimental FSI Study of Adaptive Shock Control Bumps," *Journal of Fluids and Structures*, Vol. 81, Aug. 2018, pp. 361–377.  
<https://doi.org/10.1016/j.jfluidstructs.2018.05.005>
- [43] Jinks, E., Bruce, P., and Santer, M., "Optimisation of Adaptive Shock Control Bumps with Structural Constraints," *Aerospace Science and Technology*, Vol. 77, June 2018, pp. 332–343.  
<https://doi.org/10.1016/j.ast.2018.03.018>
- [44] Ren, K., Gao, C., Zhou, F., and Zhang, W., "Transonic Buffet Active Control with Local Smart Skin," *Actuators*, Vol. 11, No. 6, 2022, Paper 155.  
<https://doi.org/10.3390/act11060155>

L. Ukeiley  
Associate Editor